*Computers and Concrete, Vol. 7, No. 2 (2010) 103-118*
DOI: http://dx.doi.org/10.12989/cac.2010.7.2.103


# Comparing finite element and meshfree particle formulations for projectile penetration into fiber reinforced concrete

James O'Daniel[1,3]*, Mark Adley[2], Kent Danielson[1], Beverly DiPaolo[1] and Nicholas Boone[1]

[1]*US Army Engineer Research and Development Center, 3909 Halls Ferry Road, Vicksburg, MS 39180-6199, USA*
[2]*US Air Force Research Laboratory, Eglin Air Force Base US Army Engineer Research and Development Center, 3909 Halls Ferry Road, Vicksburg, MS 39180-6199, USA*
[3]*ATTN: CEERD-GS-M*

*(Received July 13, 2009, Accepted September 15, 2009)*

**Abstract.** Penetration of a fragment-like projectile into Fiber Reinforced Concrete (FRC) was simulated using finite element (FE) and particle formulations. Extreme deformations and failure of the material during the penetration event were modeled with multiple approaches to evaluate how well each represented the actual physics of the penetration process and compared to experimental data. A Fragment Simulating Projectile (FSP) normally impacting a flat, square plate of FRC was modeled using two target thicknesses to examine the different levels of damage. The thinner plate was perforated by the FSP, while the thicker plate captured the FSP and only allowed penetration part way through the thickness. Full three dimensional simulations were performed, so the capability was present for non-symmetric FRC behavior and possible projectile rotation in all directions. These calculations assessed the ability of the finite element and particle formulations to calculate penetration response while assessing criteria necessary to perform the computations. The numerical code EPIC contains the element and particle formulations, as well as the explicit methodology and constitutive models, needed to perform these simulations.

**Keywords:** Fiber Reinforced Concrete; finite element; meshfree; penetration.

## 1. Introduction

Fiber Reinforced Concrete (FRC) has become an important material in protecting structures, and methods are being developed for simulating high-rate blast and impact events against FRC. This paper examines several numerical methods used to model the penetration of a Fragment Simulating Projectile (FSP) into FRC plates. Parameters were chosen to generate extreme deformation and failure of the material, including generation of a crater and perforation through the target. The penetration event was modeled with several formulations to evaluate how well each modeled the penetration process. Meshfree methods were used to evaluate their capabilities against a more traditional finite element (FE) approach using element erosion to maintain simulation stability, avoid mesh entanglement, and allow the calculation to progress through the entire penetration event. The results were then compared to experimental data to assess the viability of the models. Good

* Corresponding author, Ph.D., E-mail: James.L.O'Daniel@usace.army.mil

comparisons allow these methods to be used in a predictive fashion against similar penetration incidents. Specific simulated results were compared to the damage caused to the projectile and the target plates, as well as the residual velocity when the projectile perforates through the target.

Meshfree methods, such as Smooth Particle Hydrodynamics (SPH) (Benz 1989, Monaghan 1992, Libersky and Petschek 1990, Lucy 1977, Gingold and Monaghan 1977) and the Reproducing Kernel Particle Method (RKPM) (Liu *et al.* 1996, Chen and Liu 2000), have been used to model the damage and failure of materials. The lack of element connectivity, as is a foundation of the finite element method, gives these particle methods an intrinsic advantage. Traditional finite element technology is based on the connectivity between elements, which is not compatible with structures failing and breaking apart. This has led to various techniques that enable finite element simulations to perform calculations of breakup of the material, including element deletion and cohesive models, which use a separation criterion and subsequent contact capabilities at element interfaces, and adaptive remeshing and/or Arbitrary Lagrangian Eulerian (ALE) methods, which attempt to have the mesh follow the breakup. Particle methods can inherently separate nodes without requiring an ad hoc technique to do so. Results from EPIC (Johnson *et al.* 2006), using simulations that started with the plate formed in part or entirely of particles or had a damaged level conversion criterion that changed finite elements to particles were benchmarked against the more traditional finite element erosion method. Both computational methods were compared to experimental data. Meshfree methods (including the one used in this study) are generally computationally more expensive then finite elements, but as computer speeds get faster and the proliferation of parallel processing becomes widespread, using the particle methods has become possible and efficient.

Modeling penetration events with finite elements has necessitated the use of element erosion so that severe mesh distortion does not occur, ultimately leading to detrimentally small timesteps. The existence of the mesh or connectivity between the elements creates difficulties when large deformations, material failure, and separation are considered. Element erosion itself is fictitious in nature. Deleting a portion of the continuum is typically based on some macroscopic criteria being reached, such as the effective plastic strain failure limit in steel. This limitation does not exist with meshfree methods. The nature of the formulation lends itself to large deformations and failure since the connectivity between entities is not absolutely set with vertices between the nodes. Allowing the nodes to freely interact with other nodes in a meshless formulation instigated its use for penetration simulations.

This study concentrates on the damage generated by the FSP to the target plates and the residual velocity when the projectile perforated the targets. To these goals, simulations using (1) finite elements with erosion, (2) a method that converts finite elements to particles via a predetermined criteria, (3) finite elements with a section of particles in the penetration area tied to the elements, and (4) an entire target plate of particles, were performed to benchmark the methods against each other and compare with experimental results.

Inherent to modeling these types of materials is the constitutive model and its parameters. Parameters for the Holmquist-Johnson-Cook (HJC) concrete model (Holmquist *et al.* 1993) were developed by several means, including a fit done using a genetic algorithm. These fits were performed against characterization test data gathered at the Engineer Research and Development Center (ERDC) (Akers *et al.* 1998). The FRC investigated was named Very High Strength Fiber Reinforced Concrete (VHSFRC) and was developed at ERDC (Akers *et al.* 1998). The unconfined compressive strength was determined through characterization tests to be approximately 157 MPa. A variety of stress- and strain-path dependent tests were performed and documented in order to

characterize the structural response of the FRC material. These tests served as a baseline for determination of the material parameters that govern the numerical model's ability to reproduce the responses of the FRC.

The FRC of interest in this study consists of a typically higher than standard strength concrete matrix ($f_c'$ =170 MPa) with fibers input during the mixing process. These fibers are typically on the order of 1.27 to 3.81 cm in length and can be a wide variety of materials – including steel and fiberglass. The arrangement of the fibers can vary from completely random throughout the volume to random placement in several layers through the thickness of the volume. This depends on the FRC generation process used.

This paper describes the numerical simulations of the penetration scenarios, the development of the constitutive parameters, the experimental setup, the development of FRC material parameters, comparison of the mechanical property responses of simple finite element models against FRC characterization test data, and finally comparison of the results from numerical simulations of the penetration tests against experimental results. This combination of experiment and simulation allows an assessment of state-of-the-art modeling techniques to reproduce the behavior of FRC when subjected to penetration loads on relatively thin panels.

## 2. Numerical model description

EPIC (Elastic-Plastic Impact Code) is an explicit, large deformation, general finite element code. EPIC has been used to solve armor penetration, earth penetration, and blast loading problems. A key feature of EPIC is its meshfree method, which is a modified version of SPH. The method naturally avoids mesh distortion and entanglement problems associated with finite elements and thus can model severe deformations in a Lagrangian framework. The method, termed the Generalized Particle Algorithm (GPA), was added (Johnson *et al.* 2000) and improved upon (Johnson *et al.* 2002) to better enable EPIC to calculate extreme material deformation and failure.

As previously stated, meshfree methods are useful for the penetration scenarios examined here because of their ability to model the separation and failure of material. A historically significant problem with the Lagrangian formulation is that the mesh connectivity is attached to the motion of the material, creating elements that are highly deformed, which can cause numerical difficulties. The use of particles overcomes this problem by having the connectivity adaptable and changing as the distance between nodes increases, i.e., the weighting function decreases as the nodal range increases. The GPA differs from a traditional SPH method, in that the GPA does not require the smoothing function to conform to a Dirac delta function (Johnson *et al.* 2000). These changes improved numerical stability for problems involving tensile stresses and improved the accuracy at boundaries and interfaces over SPH (Johnson *et al.* 2002). This GPA approach differs from a finite element method basically in functions used to calculate strains, strain rates, and nodal forces. The basis of both methods (finite and meshless) in the Lagrangian formulation allows the particles to be linked to finite elements. Since computing a mesh entirely composed of particles is much more computationally expensive than one of finite elements, a model comprised of both elements and particles was generated. This includes procedures for explicitly defining different parts of the domain as particles or elements at the start of the calculation or allowing elements to convert to particles upon reaching some criteria.

Conversion of elements to particles involves the placement of a particle with the same mass and

velocity as the original element at the center of gravity of that element. Once converted, contact algorithms control the interaction between particles and elements. Motion is imparted to the particle based on the former element's momentum, and the stress state of the element is moved to the particle. All of the kinematic and stress-state variables are contained at the node for the particle. Each particle also has a support size or influence distance over which it interacts with other particles. Once a particle leaves the influence of another particle, there is no longer interaction between them (Johnson and Stryk 2003). This allows breakup and fracture of the material through the GPA without the constraint of element connectivity or the need for element erosion. Separation is governed by the support size given to each particle and while still numerical in nature, seems to generate a better approximation than erosion of elements. The changing of the element, either to remove it by erosion or convert it to a particle, was performed at the prescribed failure strain of the material. Material failure in the particle-only model is controlled naturally by the formulation, the material properties of the target, and the motion of the particles.

The models generated for this study included a mix of finite elements and particles, with some models consisting entirely of finite elements, some entirely of particles, and some using a volume of particles in the impact area and surrounded by finite elements. The variations depended on two basic parts of the formulation – what type of element did the initial mesh contain, elements and/or particles, and when elements were used, what happened to those elements upon reaching the failure criteria, i.e., were they eroded or converted to particles. Fig. 1 shows example initial meshes for a target plate for each of these model types. The target plates are described below in the experimental setup. Cases initially containing only finite elements employed either erosion or conversion criteria in order to examine the differences that resulted. When erosion was used, the finite elements were removed from the simulation upon reaching a specified strain, while for the conversion case the finite elements were changed to particles at that specified strain level. The

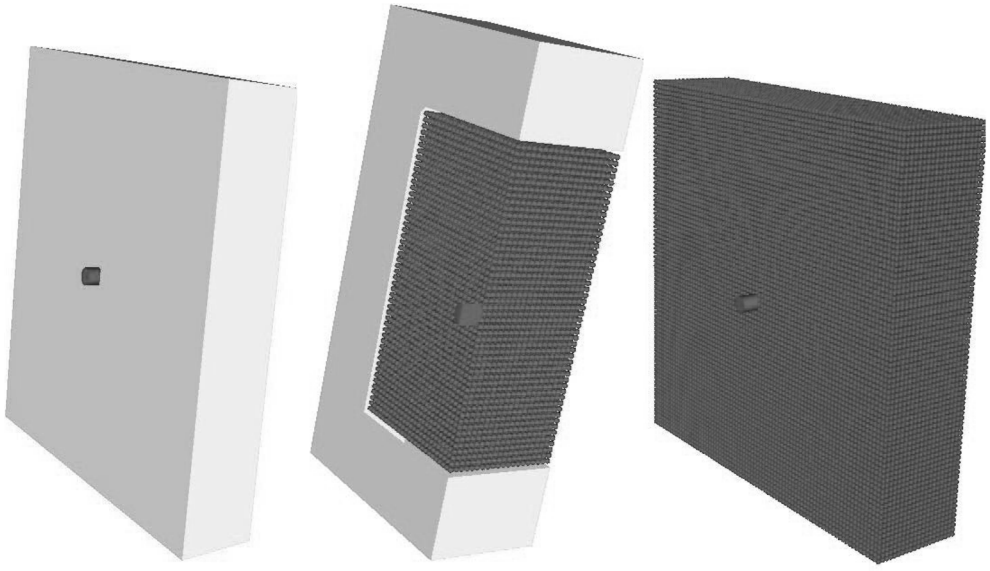


Fig. 1 (a) Finite element mesh, (b) Finite Element/Particle mesh, and (c) Particle mesh

projectile remained initially modeled with finite elements throughout the simulations, and conversion of the projectile elements to particles was allowed to occur if and when the material failure level was reached.

Contact between various entities is very important to this problem. Tracking the contact between the FSP and target initially and then between parts of both the FSP and target as they fail into possibly hundreds of pieces is a complicated process. EPIC provides robust contact for all of those cases. Comprehensive searching is performed to determine if contact has occurred and the extent of that contact. Contact is defined automatically and requires three steps: interface determination, searching, and the contact itself (Johnson *et al.* 2000). EPIC contact uses a master-slave approach, checking at each timestep for slave node penetration of master segments. Multiple conditions are checked, and once penetration has been determined, the contact algorithm is invoked. This adjusts the positions and velocities of the slave and master surface nodes in an attempt to have the slave node on the master surface with a normal velocity equal to the normal velocity of that surface.

Nodal fixity was applied to the edges of the mesh to represent the conditions applied in the experiments. Automatic contact was specified to globally capture the interaction between the penetrator and the target plate. This contact algorithm also ensured that any interaction between failed portions of the plate would be included in the response. EPIC restricted the simulation to half symmetry when the mesh was a mix of elements and particles. Any rifling of the projectile (spin about its axis) was not incorporated into the calculations. Fig. 2 shows several views of the FSP, including a picture of the actual FSP and the discretization of the projectile in the full and half-symmetry configurations.

Each FSP was made from 4340 steel, and textbook (Harvey 1982) values were used (including density of 7,833.4 kg/m$^3$, a yield strength of 1,482.4 MPa, an ultimate strength of 1,578.9 MPa, a failure strain of 16.0%, and a Young's Modulus of 207,000 MPa) in the simulations as coupon tests were not performed for the materials. Steel was simulated with a Johnson-Cook material (Johnson and Cook 1983) model, which is purely empirical and gives the following relation for the flow stress.

$$\sigma_y = [A + B(\varepsilon_p)^n][1 + C\ln(\dot{\varepsilon}_p)][1 - (T^*)^m] \quad (1)$$

where $\varepsilon_p$ is the equivalent plastic strain, $\dot{\varepsilon}_p$ is the plastic strain-rate, T is temperature, $\sigma_y$ is the flow

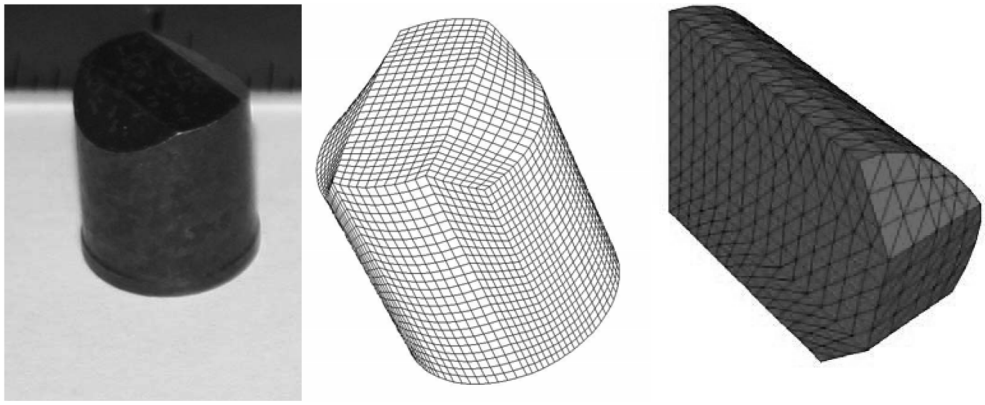

(a) (b) (c)

Fig. 2 Views of FSP (a) actual, (b) full, and (c) half symmetry

stress, and A, B, C, n, m are material constants that describe the flow stress as a function of strain hardening, strain-rate, and thermal softening. For these simulations, the 4340 coefficients were: A=1490.0 psi, B=627.0 psi, C=0.006, m=1.19, and n=0.16.

FRC was modeled using the HJC constitutive model, which contains strength, damage, strain rate effects, and a hydrostatic pressure-volume relationship. Volumetric strain, effective plastic strain, and pressure all contributed to the damage calculated within the material. The HJC model was developed for large strain, high strain-rate, and high pressure problems, such as the response to blast or impact loading. The aspects of the HJC model include (1) strength as a function of pressure, strain-rate, and damage, (2) pressure as a function of volumetric strain, and (3) damage is accumulated as a function of volumetric strain, equivalent plastic strain, and pressure. The volumetric and deviatoric responses are calculated separately. The pressure volume relationship is established based on three regions, i.e., an initial linear elastic area up to a crush pressure, a transition region between the crush pressure and the locking pressure, and the third region where the air voids have been completely removed and the material is "locked". Fibers were not explicitly modeled within these simulations, and their contribution is included in the HJC constitutive parameters developed for the entire fiber-matrix material.

General characteristics of the concrete included a density of 2.47 g/cm$^3$, an initial elastic bulk modulus of approximately 22.1 GPa, a Young's Modulus of 36.2 GPa, a shear modulus of 14.8 GPa, and a Poisson's Ratio of 0.23 (Akers *et al.* 1998). Determination of the parameters for the HJC model for the VHSFRC material is described in the following section.

## 3. VHSFRC parameter development

Characterization data is typically gathered from basic laboratory tests on a material to determine its strength and constitutive properties. Multiple stress and strain paths are followed to determine these constitutive properties. These tests include unconfined compression (UC), triaxial compression (TXC), uniaxial strain (UX), and uniaxial strain followed by constant axial strain unloading (UX/BX). All of these tests were performed quasi-statically with strain rates on the order of $10^{-4}$ to $10^{-5}$. Expanded detail on these tests can be found in Akers *et al.* 1998. Recommended properties were generated and presented in that report, and it is against those data that the constitutive model parameters were developed. The static failure surface necessary for constitutive models is derived from the TXC characterization test results, as it cannot be directly found from an individual test. It can be checked against the unloading portion of the UX/BX test. This latter test is conducted in two stages. An initial axial loading (UX) is followed by an unloading that keeps the axial strain constant as the radial strain changes.

Once these characterization data were obtained for the VHSFRC, parameters for the HJC constitutive model were derived. A spreadsheet and simple equation hand fitting was used to determine a best fit for the pressure-volume relationship and the failure surface based on the equations provided in the HJC model. As data were not available for high strain-rates, those parameters were used from previous research on regular strength concrete (Malvar and Crawford 1998).

As an improved approach, Continuous Evolutionary Algorithms (CEA) (Furukawa *et al.* 2002) in conjunction with the method of steepest descent (Kreyszig 1988) was used to determine a set of parameter values to be used in the HJC model for the FRC. These algorithms are used to minimize the weighted sum of squared residuals merit function given by Eq. (2).

$$\Phi(\bar{a}) = \sum_{i=1}^{n} w_i[\sigma_i - \hat{\sigma}_i(\varepsilon, \bar{a})]^2 \tag{2}$$

where $\sigma$ represents the stress values measured in material property experiments, $\hat{\sigma}$ represents the stress values predicted by the material model that are a function of the strain ($\varepsilon$) and the vector of material model parameter values ($\bar{a}$), and $w$ is a weighting factor. The set of parameters is set forth, and the user has control over which are varied by the CEA and over what range those parameters are varied, allowing well identified and bounded parameters to be easily traced within the CEA.

In CEA, a trial solution is a vector representation of the parameter set ($\bar{a}$). The algorithm employed in this work selects a number ($m$) of initial trial solutions where the parameter values in each of the $m$ vectors are selected at random. The following operations are then completed in a loop that is only terminated when a convergence criterion is satisfied, i.e., the merit function has reached an acceptably small value.

The operations performed each time through the loop (in each generation) in the order of calculation are (1) evaluate the merit function ($\Phi$) for each of the $m$ trial solutions (individuals), (2) identify and save the solution that provided the smallest value of the merit function for use in the next generation (the most fit individual), (3) use the method of steepest descent, starting at the best solution (the elite individual identified in the previous operation) to determine a new trial solution that will replace the worst solution (least fit individual), (4) recombine the current trial solutions to obtain the additional (m-1) trial solutions required, where the probability of a vector's participation in the recombination (mating) process depends on its merit function value (fitness). These CEA algorithms are inspired by biological evolution processes.

The recombination (mating) algorithm used in the current work is represented by the following equations.

$$\begin{aligned} \bar{a}_i^* &= (1-\alpha)\bar{a}_i + \alpha\bar{a}_j \\ \bar{a}_j^* &= \alpha\bar{a}_i + (1-\alpha)\bar{a}_j \end{aligned} \tag{3}$$

where $\alpha$ is a scalar value that is defined by a normal distribution with a mean of 0 and a specified standard deviation, and the parents ($\bar{a}_i$ and $\bar{a}_j$) are selected at random from the mating pool. Since the probability of a solution (individual) being selected to participate in the mating process depends on the value of its merit function (level of fitness), this search algorithm moves toward a solution that minimizes the merit function and provides a best fit to the material property data used in the merit function.

Once parameters were established, an initial test of the capability and robustness of the constitutive model was performed to reproduce the behavior seen in the characterization tests using the same numerical code used for the penetration simulations. Single element simulations (SES) were performed using the stress and strain paths from the characterization tests (UC, UX, etc.). Output from these simulations was then compared to the experimental data to determine if the constitutive model and the generated parameters reproduced the responses seen in the experimental characterization tests. While the correlation is not exact – comparing the response of a single element against the results from a test on a physical specimen of some size –, the comparison of the SES results against the response of a model using global parameters provides an estimate of how

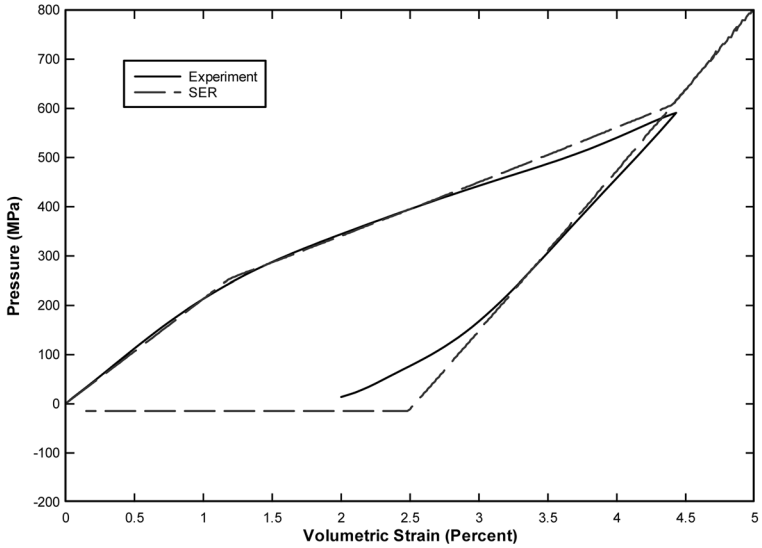


Fig. 3 Hydrostatic Compression (HC) Data

well the model reproduces general behavior of the material.

### 3.1. Concrete parameters

Figs. 3 through 6 show derived experimental results compared against the SES results for characterization tests HC, UC, UX/BX, and UX, respectively, generated using the parameters developed by the CEA algorithm. Experimental data is listed by numbers used in Akers *et al.* 1998. Above 550 MPa, a change in bulk modulus can be seen in the numerical HC curve (Fig. 3) as it was loaded above void closure, and then unloaded down the unloading part of the curve. The HC and UC comparisons are very good, and the unloading part of the SES UXBX curve, indicated in the box, overlays the experimental, inferring that the failure surface is correctly modeled. The UX case (Fig. 6) does not exhibit very good comparisons, as the calculated stress increases slightly at lower strain levels than seen in the experiments. These generated parameters reproduced most of the behavior of the VHSFRC.

## 4. Experimental description

The small arms ballistic testing facility at the ERDC consists of an underground ballistic range and an outside support building. The outside support building houses a cartridge preparation area that includes the proper equipment to hand-load numerous varieties of cartridges. The maximum range from muzzle to target is 8.62 m. The range from muzzle to target in this experimental program was approximately 4.57 m. A Modern Bond Universal small-arms receiver with a sliding return-to-zero base, shown in Fig. 7, is used to fire the projectiles. It can accommodate several barrels ranging from .22 caliber to .50 caliber.

Projectile velocity measurements were made using a pair of Oehler Research, Inc. model 35P

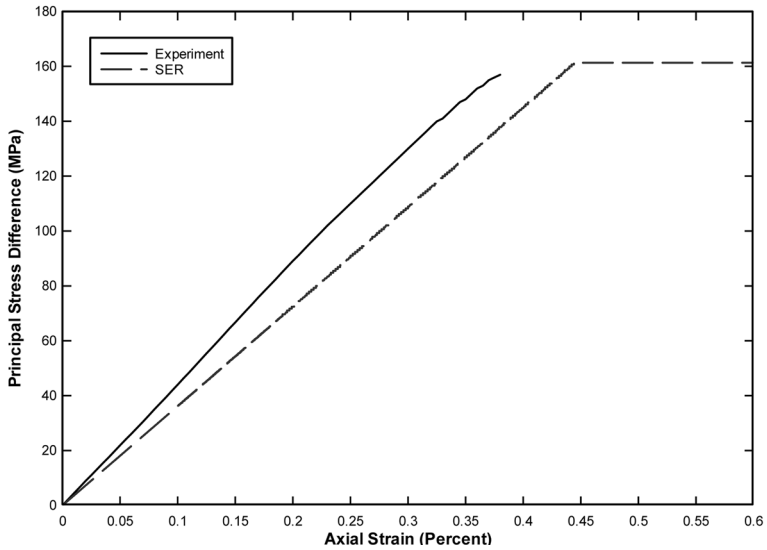


Fig. 4 Unconfined Compression (UC) Data

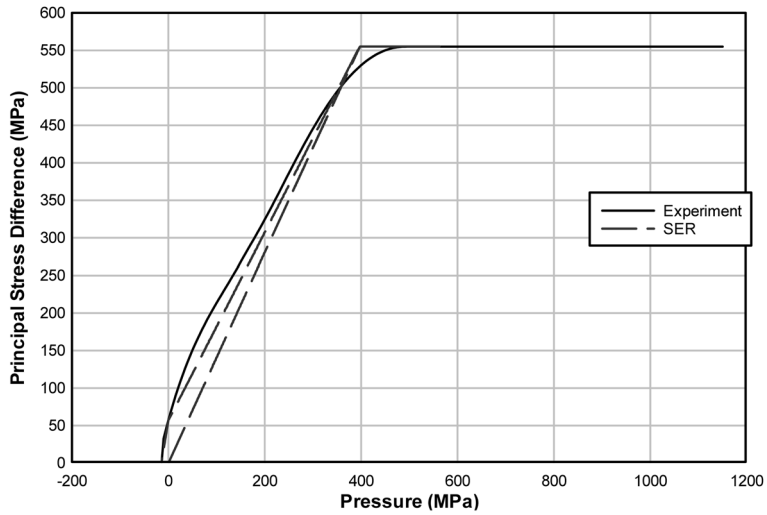


Fig. 5 Uniaxial strain loading/constant strain unloading (UX/BX) data

proof chronographs, each connected to two Oehler model 55 light screens. The light screens attached to each chronograph were positioned 0.91 m apart to measure fragment velocities. To measure entrance and exit (residual) velocities for each experiment, pairs of chronograph screens (Fig. 8) were positioned so that each pair's midpoint was located approximately 1.68 m ahead of and 1.37 m behind the test specimens.

Penetration experiments were conducted to measure the FRC's resistance to ballistic projectile penetration. Plates tested were of uniform 304.8 mm by 304.8 mm size with approximate thicknesses of 3.81, 6.35, 9.53, and 12.70 mm. When possible, test panels were rotated 180 degrees after the first penetration test, and then tested a second time near the opposite diagonal corner of the panels. The

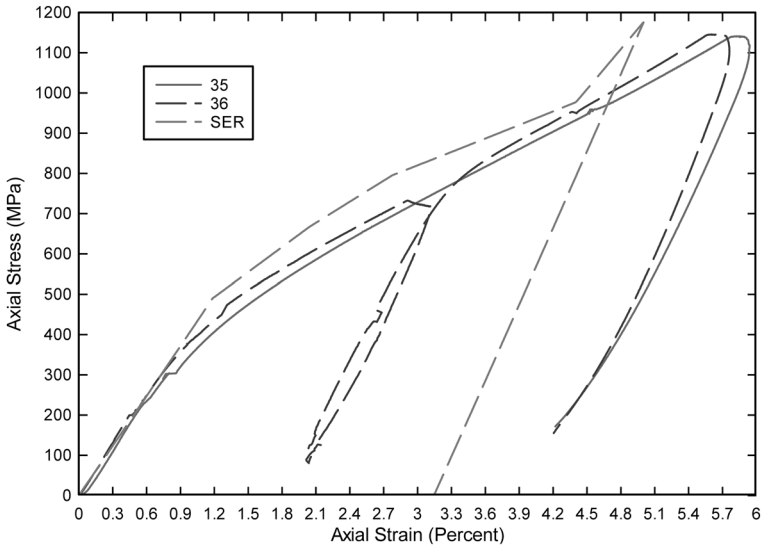


Fig. 6 Uniaxial strain (UX) data

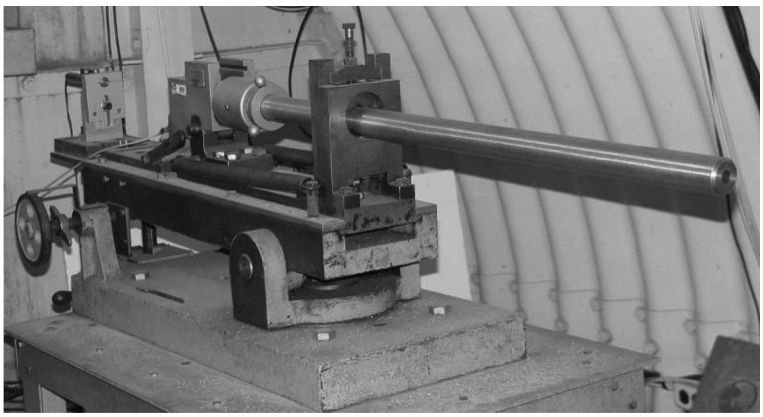

Fig. 7 Modern bond universal small-arms receiver used to fire the projectiles

effects of the penetrator were localized, and the relatively small damaged zone allowed multiple shots to be performed on each plate. Qualitative observations were also made with posttest inspection of the plate and witness panel. These observations were documented with digital photography to capture the effects of material fragments on the exit or "safe" side of the panels.

Each FSP was a 0.50 caliber projectile constructed of 4340 steel (with the basic properties listed above), was approximately 14.7 mm in length, had a diameter of about 12.7 mm, and weighed 207 grains (13.41 g). A photograph of a pristine FSP is shown above in Fig. 2. This FSP was designed to simulate a typical metal fragment from a detonating cased munition. The nominal impact velocity was 1,112 m/sec, with the actual impact velocity measured by the breaking of the chronograph planes by the FSP before striking the target. Impact velocities were as close as the variance between tests allowed. Those measured velocities were used as the input velocities in the simulations.

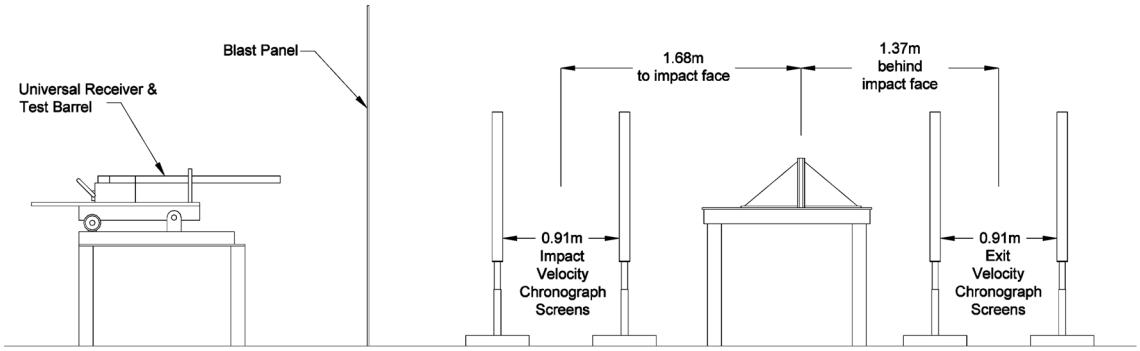


Fig. 8 Schematic of ballistic penetration test

## 5. Comparison of results

Two cases were considered for comparison of experiment and simulation, one that generated an impact side crater without perforation, and one where the FSP perforated the target. These cases were selected to represent significant and catastrophic damage final states. Comparisons are made through the geometric shapes of the craters and holes generated in the target plates and the residual velocity of the FSP in the perforation case. Damage comparisons are subjective, as the physical hole in the target does not provide any details as to the condition of the concrete surrounding that hole. Material that was described as fully damaged by the numerical model (and was subsequently eroded) may be concrete that is still barely holding together around the penetration hole. The hole size comparisons reported are between what is visible in the numerical model and what was reported from the experiment regardless of concrete condition surrounding the hole.

Fig. 9 shows the experimental final front and back states for the 5.08 cm thick target perforated by the FSP, while Fig. 10 shows the numerical results when element erosion was used. All following numerical plots show contours of the HJC damage parameter unless otherwise indicated. For each plot, red represents high damage level, while blue indicates areas of low or no damage. As discussed, comparisons of "damage" can be difficult and are subjective, since damage is not a definitive measurable parameter. Qualitatively, the damage is similar between test and calculation, but there is a larger penetration hole and more cracking in the simulation than were present in the test.

Four different numerical results were obtained using erosion, element conversion, the combination of elements and particles, and particles only (Figs. 10 through 13, respectively). These simulations were carried out to a point in time when the FSP had perforated the target, so further damage to the target may occur as a result of momentum imparted. Particles are still moving at high velocities away from the main portion of the target plate at the times shown (this is seen clearly in Fig. 12). When element erosion is used (Fig. 10), the hole is definitively larger than the experimental results (hole characteristics and residual velocities for all the cases are compared in Table 1). Experimental results were directly measured from the posttest panels. Also, while the vertical and horizontal cracking from the simulations are very similar to those from the experiment, significant diagonal cracking is seen in the numerical results that are not clearly present on the surfaces of the experimentally tested target plates. The FSP can be seen in all the numerical result plots. While the damaged volume (Fig. 10) does extend around the hole (indicated by the lighter colored areas in the figs), the front and back face spalling around the edges of the generated hole is not captured well

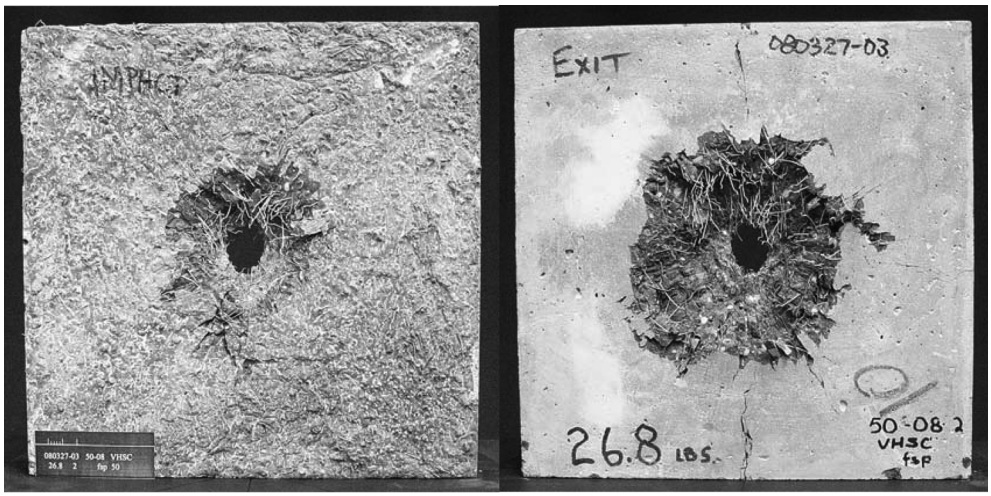


(a) (b)

Fig. 9 Experimental Results for 5.08 cm thick VHSFRC panel (a) impact side, and (b) back

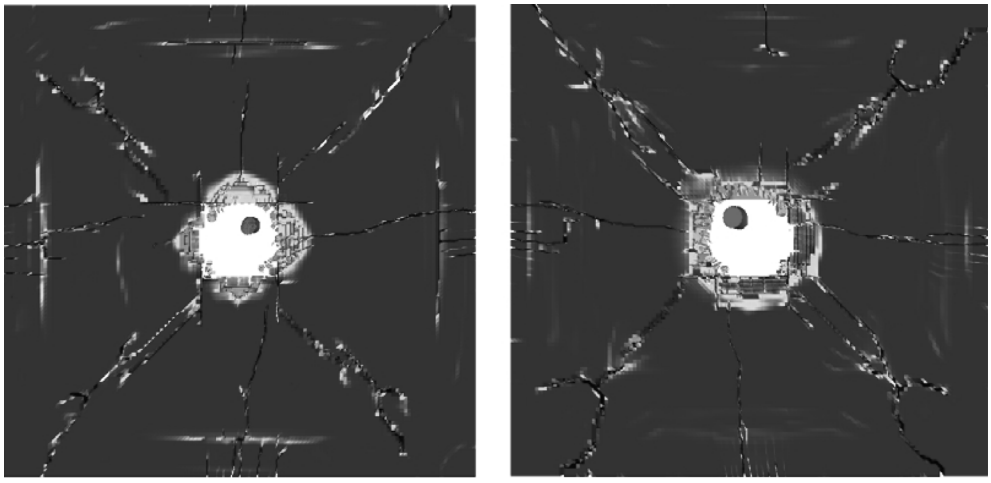

(a) (b)

Fig. 10 Simulated Results for 5.08 cm thick VHSFRC panel using element erosion (a) impact side, and (b) back

compared to the large areas seen in the test. Fig. 11(a) shows the response when the elements are converted to particles. The converted particles were visually removed during postprocessing in Fig. 11(b), generating results similar to those seen when erosion was used. When the mesh was initially defined as a volume of particles surrounded by finite elements (Fig. 12), the resulting hole was similar in character to the others, and significant particle expulsion was seen. Cracking did not extend as clearly into the finite element section of the mesh beyond the discontinuity where particles were attached to elements.

Residual velocity of the FSP was lowest for this case, 21,000 cm/sec (Table 1). All of the residual velocities were much higher than the experimental result of 3,535 cm/sec. By using only particles (Fig.

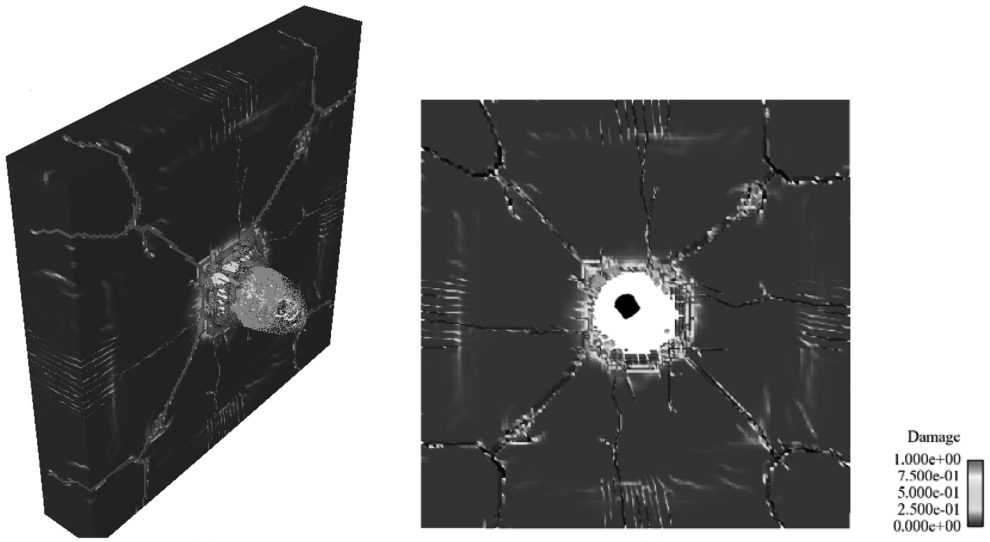


Fig. 11 Element Conversion Numerical results, (a) entire response, and (b) particles visually removed

Table 1 Resulting velocities and damage sizes

| | Thin Target (5.08 cm) | | Thick Target (7.62 cm) | |
|---|---|---|---|---|
| Formulation | Residual Velocity (cm/sec) | Hole Diameter (cm) | Crater Exterior Diameter (cm) | Crater Depth (cm) |
| Conversion | 26,238 | 7.29 | 6.17 | 4.90 |
| Erosion | 21,130 | 4.97 | 5.03 | 3.18 |
| Combined | 21,003 | 9.22 | 7.19 | 4.65 |
| Particles | 24,848 | 6.78 | - | - |
| Experimental | 3,535 | 3.43 | 11.10 | 2.66 |

13), the computational time was increased by a factor of approximately five over the case where conversion was used to compute to the same simulation time. A final residual velocity of 24,800 cm/sec was seen for this case, and the diagonal cracking was similar to the erosion and conversion cases.

As a test of the ability of the different methods to simulate partial penetration without perforating the target, a 7.62 cm thick plate was tested. Fig. 14 shows a comparison of the conversion formulation results and the experimental results. Gross damage compares qualitatively well between experiment and simulation. Crater dimensions are smaller at the face of the target, but the FSP penetrated deeper into the target, as indicated in Table 1. The simulation showed some of the concrete slightly pushing out from the back side (~0.2 cm), which was more than the experiment showed. When the combination of particle and FE volumes was used, a significantly larger hole was generated in the simulation than in the experiment (Fig. 15), indicating this FRC representation of the target was too soft and allowed the FSP to perforate through the target, unlike what was seen in either the experiment or when using the conversion formulation. Particles that had a high velocity were visually removed, generating the hole seen in Fig. 15.

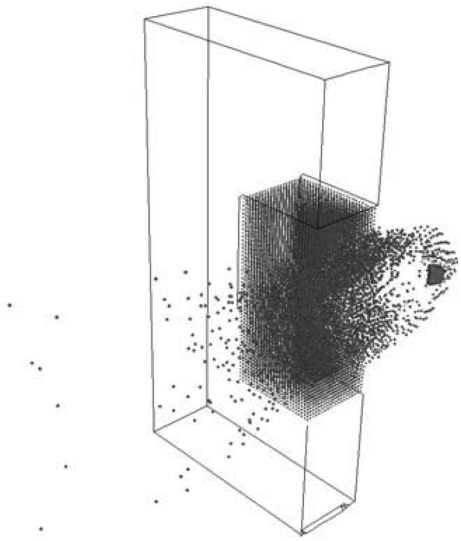

Fig. 12 Combined Particle and FE mesh outline and resulting particle response

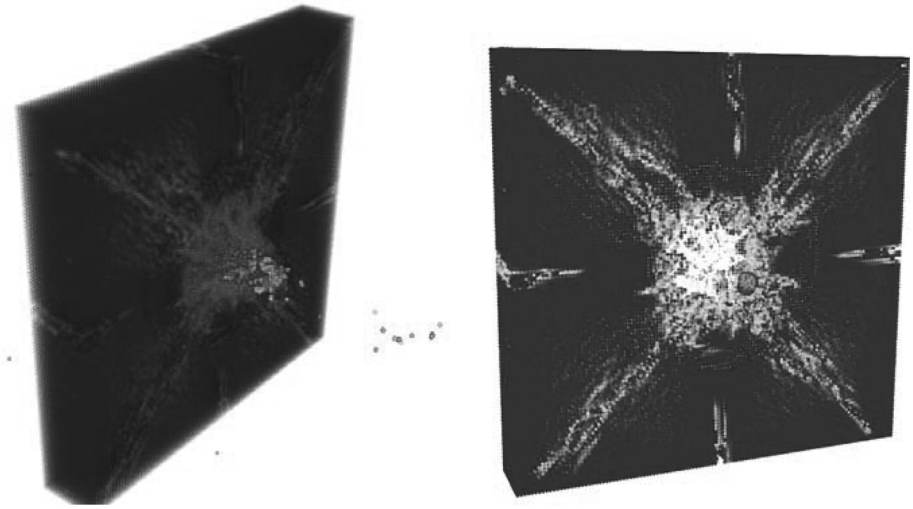

(a) (b)

Fig. 13 Particle-only mesh (a) total response, and (b) particles with Damage > 1.0 visually removed

## 6. Conclusions

Multiple formulations were used to compare against experimental results for the penetration effects of an FSP into fiber reinforced concrete. This allowed the comparison of finite element (and the failure mechanisms for them) with a particle-based method that inherently can simulate large strain and failure type behavior. Using failure criteria within the HJC model that had been determined through previous comparisons of test and simulation, the damage compared qualitatively well between the FE formulations and the experimental results, but the residual velocities were extremely overestimated. All the simulations exhibited diagonal cracking that was not visible in the

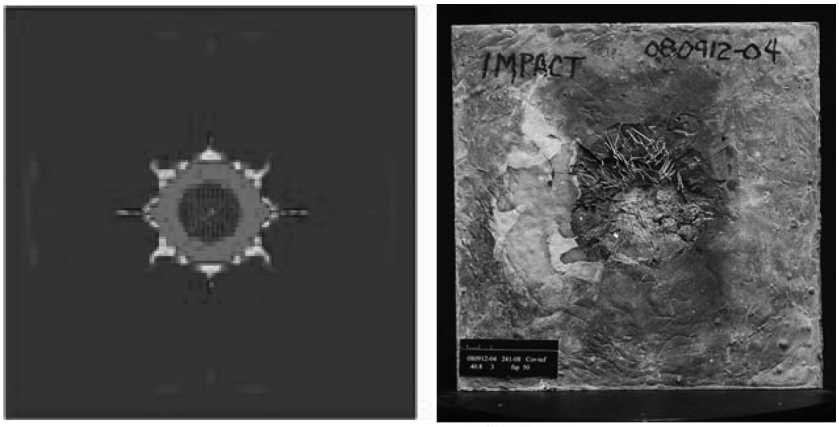


(a) (b)

Fig. 14 Comparison of (a) the conversion simulation and (b) the experimental results for the 7.62 cm thick FRC panel

Fig. 15 7.62 cm thick FRC panel simulated results for a combination of particle and FE

experimental results. Using a mesh that was initially comprised of finite elements and converting those elements to particles generated the best results when considering four factors, i.e., damage to the target, post-perforation FSP velocity, mass conservation within the simulation, and computational efficiency of the method compared to the use of an initial particle domain. Although the mechanical property simulations of the FRC compared well against the laboratory mechanical property data, a deficiency was shown in achieving quantitatively adequate simulated results for the FSP penetration of FRC panels.

This study generated a baseline of current capabilities to model a high rate, large deformation, and failure of fiber reinforced concrete problems. Significant work still remains in the areas of discretization convergence for particle size and the relation of particle and FE meshes when both are used in the same simulation. Accuracy of the strain-rate parameters used in this study is an open issue that needs to be addressed to determine if the model that was used was accurate, and if not,

what should be used instead. Several questions remain that are the focus of current efforts, including: "Is the larger hole size in the simulations due to the inability of the numerical and constitutive models to hold the concrete together after microcracking occurs?", "Will adding the contribution of the fibers enable better numerical modeling of the failure behavior?", and "Do the fibers need to be explicitly modeled in order to better capture the response of FRC and generate a closer approximation of the residual velocity when perforation occurs?"

## Acknowledgements

Simulations in support of this project were performed on the systems of the DoD Supercomputer Resource Center at the Engineer Research and Development Center. Permission to publish was granted by Director, Geotechnical and Structures Laboratory.

## References

Akers, S.A., Green, M.L. and Reed, P.A. (1998), "Laboratory characterization of very high-strength fiber-reinforced concrete", US Army Corps of Engineers, Waterways Experiment Station TR SL-98-10.

Benz, W. (1989), *Smooth particle hydrodynamics: a review*, Harvard-Smithsonian Center for Astrophysics (Preprint 2884).

Chen, J.S. and Liu, W.K. (2000), "Meshfree particle methods", *Comput. Mech*., **25**(2).

Furukawa, T., Sugata, T., Yoshimura, S. and Hoffman, M. (2002), "An Automated system for simulation and parameter identification of inelastic constitutive models", *Comput. Method. Appl. M.,* **191**, 2235-2260.

Gingold, R.A. and Monaghan J.J. (1977), "Smoothed particle hydrodynamics: theory and application to non-spherical stars", *Mon. Not. R. Astron. Soc*., **181**, 375-389.

Harvey, P.D. (1982), *Engineering Properties of Steel,* American Society for Metals.

Holmquist, T.J., Johnson, G.R. and Cook, W.H. (1993), "A computational constitutive model for concrete subjected to large strains, high strain rates and high pressures", *Fourteenth International Symposium on Ballistics*, Quebec City, Canada, September.

Johnson, G.R., Beissel, S.R., Gerlach, C.A., Stryk, R.A., Holmquist, T.J., Johnson, A.A., Ray, S.E. and Arata, J.J. (2006), "User Instructions for the 2006 Version of the EPIC Code", *Final Report, Contract DAAD19-03-D-0001*, U.S. Army Research Laboratory.

Johnson, G.R., Beissel, S.R. and Stryk, R.A. (2000), "A generalized particle algorithm for high velocity impact computations", *Comput. Mech.,* **25**, 245-56.

Johnson G.R., Beissel S.R. and Stryk R.A. (2002), "An improved generalized particle algorithm that includes boundaries and interfaces", *Int. J. Numer. Meth. Eng.,* **53**, 875-904.

Johnson, G.R. and Stryk, R.A. (2003), "Conversion of 3D distorted elements into meshless particles during dynamic deformation", *Int. J. Numer. Meth. Eng,* **28**(9), 947-966.

Johnson, G.R. and Cook, W.H. (1983), "A constitutive model and data for metals subjected to large strains, high strain rates, and high temperatures", *Seventh International Symposium on Ballistics*, The Hague, The Netherlands.

Kreyszig, E. (1988), *Advanced Engineering Mathematics,* Sixth Edition, John Wiley & Sons, NY, 1112-1115.

Libersky, L.D. and Petschek, A.G. (1990), "Smooth particle hydrodynamics with strength of materials", *Adv. Free Lagrange Method, Lecture Notes Physics*, **395**, 248-257.

Liu, W.K., Belytschko, T. and Oden, J.T. (1996), "Meshless Methods", *Comput. Method. Appl. M.*, **139**(1).

Lucy, L.B. (1977), "A numerical approach to the testing of fusion process", *Astron. J.* **88**, 1013-1024.

Malvar, L.J. and Crawford, J.E. (1998), "Dynamic increase factors for concrete", *Proceedings for the 28th DoD Explosive Safety Board Seminar*, Orlando, FL.

Monaghan, J.J. (1992), "Smoothed particle hydrodynamics", *Annu. Rev. Astron. Astr.,* **30**, 543-574.